J. Fluid Mech. (1994), *vol.* 275, *pp.* 33–57

The boundary-layer flow due to a vortex approaching a cylinder

By H. AFFES, Z. XIAO AND A. T. CONLISK
Department of Mechanical Engineering, The Ohio State University, Columbus, OH 43210, USA

(Received 11 January 1994 and in revised form 15 March 1994)

The three-dimensional unsteady boundary layer induced by a vortex filament moving outside a circular cylinder is considered. In the present paper, we focus attention on the situation where the inviscid flow is fully three-dimensional but is symmetric with respect to the top centreline of the cylinder. The motion of the vortex toward the cylinder leads to separation of the boundary layer; in the present work a large unsteady adverse pressure gradient develops as well. Results for the three-dimensional streamlines, the vorticity distribution, and the velocity component normal to the cylinder indicate the presence of a region of unsteady three-dimensional secondary flow structure of rather complex shape located deep within the boundary layer. Within this three-dimensional secondary flow the fluid is progressively squeezed into a narrow region under the main vortex and it is expected that a local three-dimensional jet will develop sending boundary-layer fluid out into the main stream. It is pointed out that such three-dimensional eruptive behaviour has been observed in experiments. The results indicate the development of a three-dimensional singularity in the boundary-layer equations.

1. Introduction

In recent years, there has been an increasing amount of attention paid to problems associated with interaction of regions of concentrated vorticity with solid boundaries and the effect of these regions on the boundary-layer flow under them. Such flows occur in a wide variety of physical situations; for example, it is now commonly accepted that vortex motions play a major role in the dynamics of wall-bounded turbulent flows. Moreover, the interaction of 'vortices' with solid boundaries is important in the study of impinging shear and mixing layers, in the study of the wakes of low-flying aircraft, in the flow within gas turbines, in the dynamic stall process and in the study of the induced load on the fuselage of a helicopter, among many others. The present work is concerned with a problem motivated by study of this last application.

The motivation for this work is the observation by Sheridan & Smith (1980) that many different aerodynamic interactions between different components can adversely affect helicopter performance. In the recent past there has been a tendency for helicopters to be more compact in size leading to tighter clearances between individual components. Consequently interactions between components have become more important in the design process. Among the most important interactions is that between the wake shed by the rotor blade(s) and the airframe. In particular, Sheridan & Smith (1980) identify vortex–surface impact to be a significant interaction because of the high-frequency impulsive loads such a process generates. The present paper is concerned with a particular type of vortex–surface impact: that of the interaction of

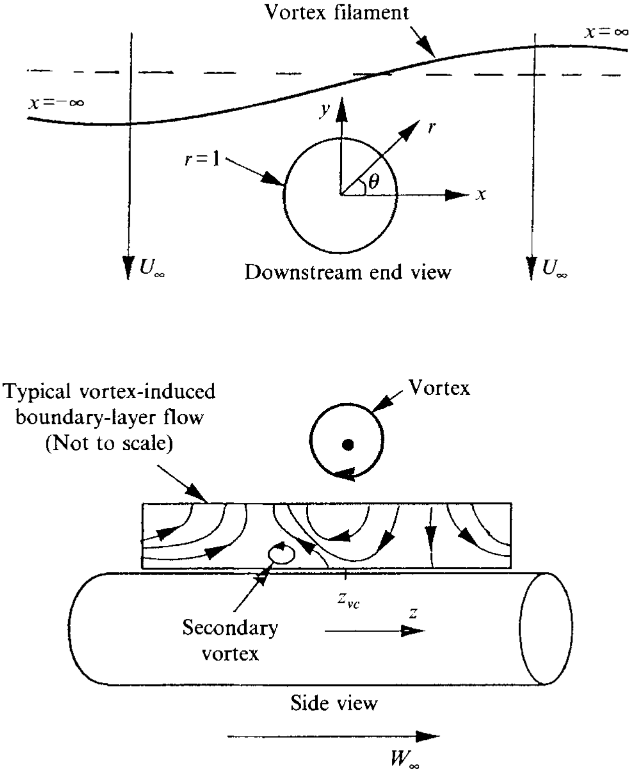

FIGURE 1. Geometry of the present work and the coordinate system employed. An expanded view of the expected boundary layer flow which is characterized by the appearance of a secondary eddy is also shown. $r = 1$ denotes the cylinder surface.

a concentrated vortex structure with a cylinder. This interaction has been considered from an inviscid point of view in previous work (Affes & Conlisk 1993; Affes *et al.* 1993) and in the present paper we consider the development of the viscous flow on the airframe in the case where there is a symmetry plane within the flow field. For simplicity we consider the airframe to be a circular cylinder and the vortex to be modelled by an infinite line vortex. This vortex geometry is an idealization of the actual case where the tip vortex shed from a helicopter blade consists of a continuous helical line of concentrated vorticity. However, the radius of curvature of the helix is most often approximately constant and is usually much larger than the average radius of the airframe; consequently as the vortex approaches the airframe, it appears as an approximately straight vortex oriented perpendicular to the generators of the cylinder.

The physical problem of interest is depicted on figure 1; in general, the initial position of the vortex may be specified arbitrarily. In the present work we consider the case where the vortex is initially parallel to the x-axis; the initial position of the vortex is specified by the dashed line on figure 1. The purpose of the present work is to compute the induced boundary-layer flow. The fluid is assumed to be incompressible inviscid and irrotational outside the core of the vortex and away from the airframe boundary. We further assume that the mean fluid motion is symmetric about the y-axis of figure 1; in experiments (Liou, Komerath & McMahon 1990; Brand, McMahon & Komerath 1990), the actual mean fluid motion is asymmetric with respect to the y-axis and this problem will be reported in future work.

The motion of a three-dimensional vortex in free space has been documented by a number of authors and an excellent discussion of the previous work in this area is given by Hon & Walker (1987) and Sarpkaya (1989). For the case where the vortex interacts with a body, the amount of work is much more limited, and only simple body shapes such as a plane wall (Hon & Walker 1987) and a sphere (Lewis 1879; Larmor 1889; Lighthill 1957; Dhanak 1981) have been considered previously; moreover, in general, the vortex shape is also restricted (Lewis 1879; Larmor 1889; Lighthill 1957).

The two-dimensional boundary-layer flow induced by a vortex has been investigated by several authors. Walker (1978) was the first to calculate the boundary layer due to a vortex in a stagnant medium. He found that the main vortex induces a separated flow under it in the sense that a reversed-flow eddy forms early in the calculation and grows in time, eventually causing a catastrophic breakdown of the numerical calculation. He also suggests that no physically acceptable steady solution of the boundary-layer flow exists even though the motion of the vortex is steady in a reference frame travelling at the vortex speed. In addition, his results suggest explosive boundary-layer growth and he postulates that the secondary vortex formed deep in the boundary layer will eventually be driven away from the wall. Doligalski & Walker (1984) were the first to describe the convecting vortex–boundary interaction and their results support the conjectures of Walker (1978) for the stagnant-medium case. Chuang & Conlisk (1989) have computed the corresponding solution using interacting boundary-layer techniques; they show that the vortex is indeed driven from the wall under the action of the boundary-layer flow as suggested by Walker (1978). They also found that a tertiary eddy is spawned late in the calculation and identified the development of a shear-layer region above the spawned secondary vortex which may be the conduit for the ejection of the secondary vortex into the outer flow. Peridier, Smith & Walker (1991*a*, *b*) consider the same problem as Walker (1978) using Lagrangian techniques and are able to carry the calculation to the singular time. A similar approach is used in the case of the interacting boundary layer. Walker *et al.* (1987), in a combined numerical and experimental study, have investigated the boundary layer due to the impact of an axisymmetric vortex ring on a wall. Ersoy & Walker (1985) and Hon & Walker (1987) have computed the boundary-layer flow due to a loop vortex and a hairpin vortex respectively, along a symmetry plane present in each case.

The vortex–boundary layer interactions described here have been observed experimentally by Harvey & Perry (1971) and more recently in the experiments described in Walker *et al.* (1987). In particular, in Walker *et al.* (1987) explosive boundary-layer growth and eventual ejection of a secondary vortex ring was observed to occur. In the rotorcraft area, fundamental experiments on a rotor–airframe configuration have been performed at Georgia Institute of Technology (Liou *et al.* 1990; Brand *et al.* 1990). These two studies have focused primarily on the behaviour of the tip vortex at locations far from the airframe.

In all the computational work described above the flow is either two-dimensional or axisymmetric, or the flow is computed in a symmetry plane; however, the present problem is fully three-dimensional in the general case where the initial configuration of the vortex is arbitrary. For simplicity, however, we confine ourselves to the situation where the initial vortex position is symmetric about the y-axis (figure 1). Even in this limiting case the presence of three-dimensionality and the unsteadiness associated with the motion of the vortex makes the analysis and computation of the solution to the problem extremely difficult. Moreover, as in the two-dimensional case, the vortex is expected to induce the formation of a secondary eddy in the boundary layer and thus the flow is likely to be separated as well.

We consider here the development of the boundary layer on the cylinder during the time frame prior to when a portion of the vortex collides with the cylinder. The problem is set up as an impulsive start; prior to time $t = 0$ a vortex is moving in a three-dimensional flow field. At time $t = 0$ a cylinder is suddenly inserted into the region and the time evolution of the boundary-layer flow is of primary interest in this work. The nature of the inviscid flow is reviewed in §2. In §3 the boundary-layer problem is formulated using classical boundary-layer theory in three dimensions. The numerical methods employed to compute the boundary-layer flow are outlined in §4. The results for the boundary-layer flow are presented in §5 and a summary and discussion of the present work appears in §6.

2. The inviscid flow problem

2.1. *Vortex advance*

The procedure to advance the vortex and to obtain the surface speeds is described in detail by Affes & Conlisk (1993) and Affes (1992) and what follows is a short summary of that work. Here, the vortex is advanced according to the evolution equation

$$\frac{\partial \boldsymbol{X}}{\partial t}(s,t) = \boldsymbol{U}, \tag{1}$$

where the timescale t is defined by

$$t = (W_\infty/a)\, t^*, \tag{2}$$

where t^* is dimensional time, W_∞ is the velocity scale, and

$$\boldsymbol{U} = \boldsymbol{U}_I + \boldsymbol{U}_V + \boldsymbol{U}_M, \tag{3}$$

where $\boldsymbol{U}_V$ is the velocity distribution induced by the vortex itself, $\boldsymbol{U}_I$ is the image distribution in the cylinder, and $\boldsymbol{U}_M$ is the mean flow distribution. The velocity $\boldsymbol{U}$ has been non-dimensionalized on W_∞ and lengths have been scaled on a which is the radius of the cylinder. Here W_∞ is taken to be the axial mean flow component and the dimensionless circulation is defined by

$$\Gamma = \Gamma^*/(W_\infty a).$$

In the present paper, the initial position of the vortex is given by $y_s = y_0, z_s = 0, f(s) = s$ where s is a parametric variable defining the vortex, and y_0 is the starting location of the vortex above the cylinder. The vortex-induced velocity $\boldsymbol{U}_V$ is defined by (Batchelor 1967)

$$\boldsymbol{U}_V(\boldsymbol{X},t) = -\frac{\Gamma}{4\pi}\int_C \frac{(\boldsymbol{X}-\boldsymbol{X}')\times \mathrm{d}\boldsymbol{X}'}{\{|\boldsymbol{X}-\boldsymbol{X}'|^2+\mu^2\}^{3/2}}, \tag{4}$$

where the curve C is the space curve which defines the position of the centreline of the vortex.

In (4) μ is a cutoff parameter which is fixed by appeal to the exact solution for the vortex ring problem (Moore 1972; Ersoy & Walker 1985) and the result is

$$\ln\left(\frac{\mu^*}{a_v^*}\right) = -\frac{1}{2} - \frac{4\pi^2}{\Gamma^{*2}}\int_0^{a_v^*} v'^2\, r^*\, \mathrm{d}r^* + \frac{8\pi^2}{\Gamma^{*2}}\int_0^{a_v^*} w'^2 r^*\, \mathrm{d}r^*,$$

where v' and w' are the azimuthal and axial velocities, respectively, in the core of the vortex, a_v^* is the dimensional vortex core radius; r^* and μ^* are also dimensional. For the case of $w' = 0$ and v' corresponding to a Rankine vortex

$$v' = \begin{cases} \Gamma^* r^*/2\pi a_v^{*2} & \text{if} \quad r^* \leqslant a_v^* \\ \Gamma^*/(2\pi r^*) & \text{if} \quad r^* \geqslant a_v^*; \end{cases}$$

then
$$\mu = a_v e^{-3/4}. \tag{5}$$

The parameter μ in (5) is dimensionless and is defined by $\mu = \mu^*/a$ here a is the cylindrical airframe radius, and $a_v = a_v^*/a$. It should be noted that if, for example, the axial velocity $w' = e^{-cr^{*2}}$, where c is a constant then μ^* can also be obtained analytically (Affes & Conlisk 1991). In this case, the effect of w' on μ^* is small since c is usually chosen to be sufficiently large in order to make w' vanish at $r^* = a_v^*$ (Affes & Conlisk 1991). Therefore, in the present work we consider only the case where $w' = 0$.

2.2. *The mean flow distribution*

In this paper, the mean flow distribution will be assumed to be symmetric with respect to the y-axis (figure 1) and correspond to the superposition of two-dimensional flow past a cylinder and a constant axial flow. Accordingly, the distribution is given by (Affes 1992)

$$U_M = \gamma \frac{\sin 2\theta}{r^2} \hat{\imath} - \gamma \left(1 + \frac{\cos 2\theta}{r^2}\right) \hat{\jmath} + \hat{k}, \tag{6}$$

where (r, θ) are standard cylindrical polar coordinates (r is made dimensionless on the cylinder radius a) and $\hat{k}, \hat{\jmath}, \hat{k}$ are unit vectors in the directions (x, y, z) (figure 1); also

$$\gamma = U_\infty / W_\infty,$$

and U_∞ is the downwash velocity as $y \rightarrow \infty$; γ is a free parameter.

2.3. *The image distribution*

The image of the vortex in the cylinder is calculated using the Fourier transform in the z- and θ-directions. Let $\phi' = \phi_I + \phi_V$, where ϕ_V is the potential due to a vortex in free space and ϕ_I is the perturbation potential due to the image of the vortex in the cylinder. Then ϕ_I satisfies

$$\nabla^2 \phi_I = 0 \quad \text{with} \quad \partial \phi_I / \partial r = -\partial \phi_V / \partial r \quad \text{at} \quad r = 1, \tag{7}$$

and ϕ_I must be bounded as $r^2 + z^2 \rightarrow \infty$. To simplify the calculations, the cylinder is assumed to be infinite in length. Using the Fourier transform in both the θ- and z-directions, we have

$$\phi_I = \frac{1}{4\pi^2} \sum_{m=-\infty}^{\infty} \int_{-\infty}^{\infty} \hat{\phi}_I e^{im\theta} e^{ikz} \, dk, \tag{8}$$

where
$$\hat{\phi}_I = -\left.\frac{\partial \hat{\phi}_V}{\partial r}\right|_{r=1} \frac{K_m(|k|\, r)}{|k|\, K'_m(|k|)}, \tag{9}$$

where K_m is the modified Bessel function of order m. Note that $\partial \phi_V / \partial r|_{r=1}$ is the radial velocity component U_{V_r} at $r = 1$. The solution for ϕ_I may be computed using fast Fourier transforms (Cooley & Tukey 1965); details are provided by Affes (1992) and Affes & Conlisk (1993).

2.4. *Surface speeds and pressure gradients*

As noted previously, in general, the flow field consists of that induced by the vortex itself, that induced by the image field due to the vortex, and a component due to any mean flow. To incorporate the mean flow given by (6) we define the total potential as

$$\phi = \phi_I + \phi_V + \phi_M,$$

where ϕ_M is the potential for the mean flow. The expression for ϕ_I given by (8) is not altered since the mean flow satisfies the solid-wall boundary condition.

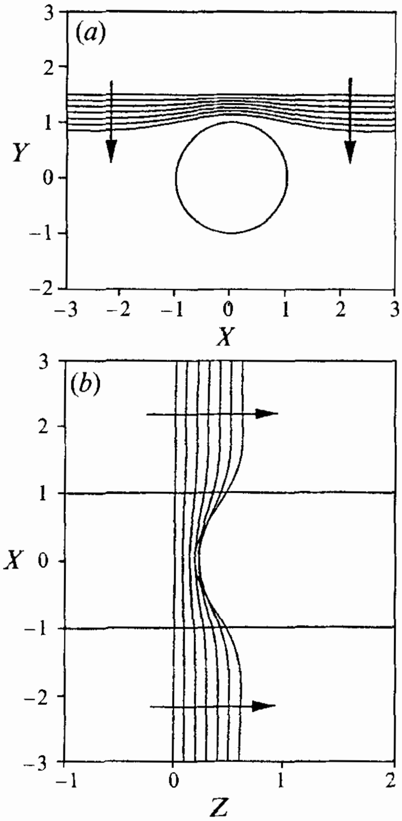

FIGURE 2. Vortex positions for several times: (*a*) end view, (*b*) top view. The initial configuration of the vortex is noted in the text. Here $\Delta t = 0.05$ and the vortex core radius $a_v = 0.11$. Arrow denotes increasing time.

Let (r, θ, Z) denote the fixed polar coordinate system; then the new coordinate system whose origin is moving with the vortex head speed U_c is given by (r, θ, z) where

$$z = Z - Z_{Vc}(t).$$

Here, Z_{Vc} is the position of the vortex head in the z-direction. Thus in a frame of reference moving with speed U_c, the Bernoulli equation for the pressure is given by

$$(\partial\phi/\partial t) + \tfrac{1}{2}|U|^2 + p + F = f_0(t), \tag{10}$$

where

$$F = -U_c(\boldsymbol{U}\cdot\hat{\boldsymbol{k}}).$$

Here f_0 is the Bernoulli constant obtained by evaluating the left-hand side of (10) at the beginning of the integration path.

Similarly, Euler's equations for the pressure gradients, in a frame of reference moving with the vortex centre speed, may be written as

$$-\frac{\partial p}{\partial \theta} = \frac{\partial U_\theta}{\partial t} + U_\theta \frac{\partial U_\theta}{\partial \theta} + (U_z - U_c)\frac{\partial U_\theta}{\partial z}, \tag{11}$$

$$-\frac{\partial p}{\partial z} = \frac{\partial U_z}{\partial t} + U_\theta \frac{\partial U_z}{\partial \theta} + (U_z - U_c)\frac{\partial U_z}{\partial z}. \tag{12}$$

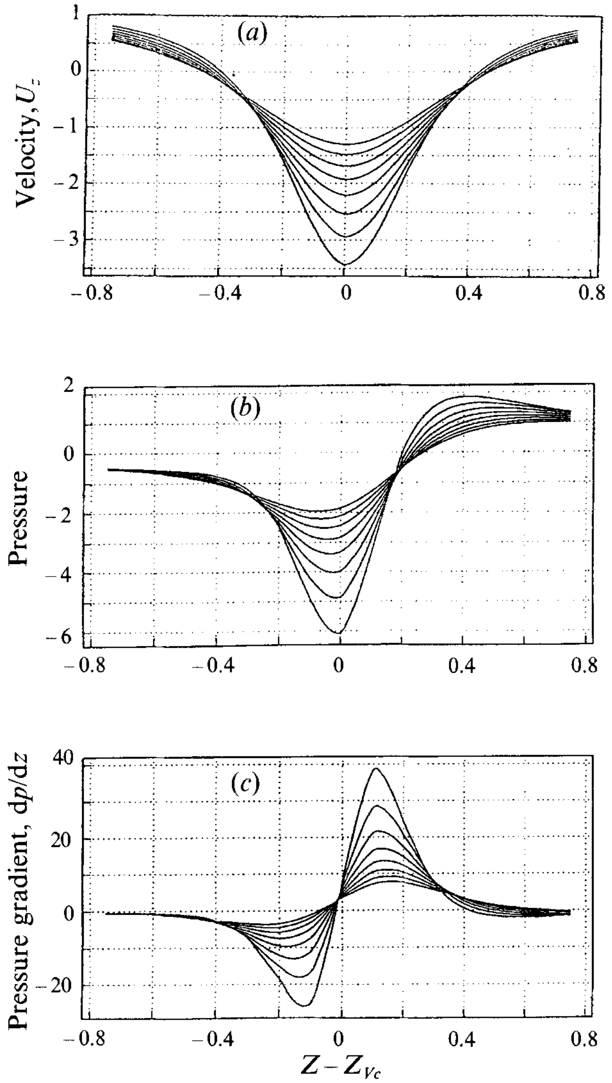

FIGURE 3. Temporal development of the inviscid flow field and the pressure at the top of the cylinder ($r = 1$ and $\theta = \pi/2$). (*a*) The velocity component U_z. (*b*) the pressure and (*c*) the pressure gradient $\partial p/\partial z$. These results are plotted at times $t = 0.05, 0.1, 0.15, \dots, 0.4$.

Details of the calculation of the surface speeds and the pressure gradients are presented in Affes (1992).

2.5. *Inviscid flow results*

For the results discussed here the initial position of the vortex is $x = s$, $y = 1.5$ and $z = 0$. There are 61 points along the vortex and the time step is $\Delta t = 0.01$. Figure 2 shows the vortex position; the vortex has a rather large dimensionless strength $\Gamma = 4.18$ and the parameter $\gamma = 1$. Note that the vortex bends in a fully three-dimensional manner owing to the presence of the airframe. It should be stated that to correspond to boundary-layer scaling, the time is non-dimensionalized differently than in the paper by Affes & Conlisk (1993). On figure 2, the total time of the calculation is $t = 0.6$ and as will be shown later the boundary-layer flow calculations cannot be continued accurately after $t = 0.4$. To investigate the properties of the inviscid flow on the top of

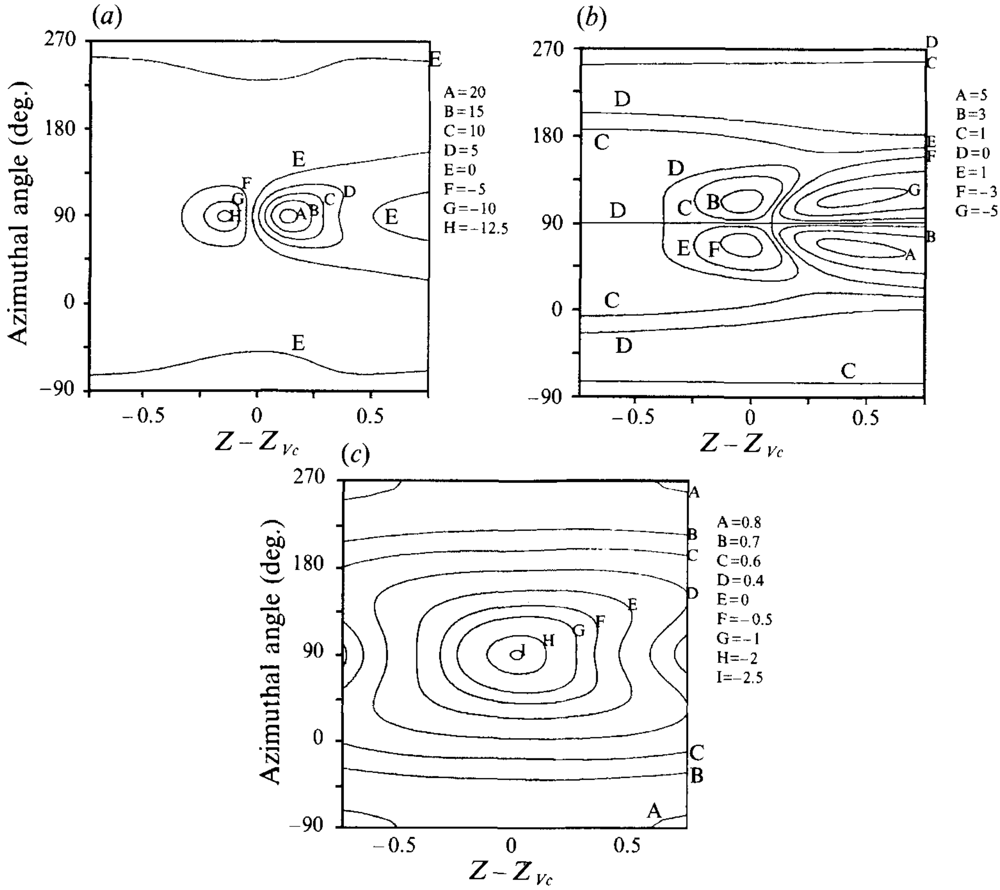

FIGURE 4. Lines of (*a*) streamwise pressure gradient $\partial p/\partial z$, (*b*) azimuthal pressure gradient, and (*c*) constant inviscid velocity U_z. $t = 0.3$.

the cylinder where flow reversal in the boundary layer is expected to be strongest, the axial velocity U_z, the pressure gradient $\partial p/\partial z$ and pressure at the symmetry plane and at various times are depicted on figure 3. The results show rapid time variation as the vortex approaches with the consequent development of a large adverse streamwise pressure gradient. Note also that the axial velocity is negative in the region under the vortex (figure 3*a*). The local nature of the adverse streamwise pressure gradients is shown on figure 4. Here it is seen that the adverse streamwise pressure gradient of value $+5$ extends downstream and is off the symmetry plane by about 30°, indicating the possibility of axially separated flow to that spanwise location. The azimuthal pressure gradient is not as severe. The streamwise velocity is negative directly under the vortex but positive at locations significantly removed from the symmetry plane. Note also the relatively local character of the rapid variation in the pressure gradients and the relatively large values of the axial velocity directly under the vortex.

3. The boundary-layer problem

The three-dimensional unsteady boundary-layer equations are given by

$$\frac{\partial u_r}{\partial y}+\frac{\partial u_\theta}{\partial \theta}+\frac{\partial u_z}{\partial z}=0, \tag{13}$$

$$\frac{\partial u_\theta}{\partial t}+u_r\frac{\partial u_\theta}{\partial y}+u_\theta\frac{\partial u_\theta}{\partial \theta}+(u_z-U_c)\frac{\partial u_\theta}{\partial z}=-\frac{\partial p}{\partial \theta}+\frac{\partial^2 u_\theta}{\partial y^2}, \tag{14}$$

$$\frac{\partial u_z}{\partial t}+u_r\frac{\partial u_z}{\partial y}+u_\theta\frac{\partial u_z}{\partial \theta}+(u_z-U_c)\frac{\partial u_z}{\partial z}=-\frac{\partial p}{\partial z}+\frac{\partial^2 u_z}{\partial y^2}, \tag{15}$$

where U_c is the convection speed of the head of the vortex in the z-direction and the axial coordinate is defined relative to the position of the vortex head and is given by $z=Z-Z_{Vc}$ where Z is the *fixed* axial coordinate. Consistent with the inviscid flow, the dimensionless variables are defined by

$$\left.\begin{aligned}\theta=\theta^*,\quad z=\frac{z^*}{a},\quad y=\left(\frac{r^*}{a}-1\right)Re^{1/2},\quad t=\frac{W_\infty}{a}t^*,\quad u_r=\frac{u_r^*}{W_\infty}Re^{1/2},\\ u_\theta=\frac{u_\theta^*}{W_\infty},\quad u_z=\frac{u_z^*}{W_\infty}.\end{aligned}\right\} \tag{16}$$

The Reynolds number is $Re=W_\infty a/\nu$, and the pressure p^* is non-dimensionalized on ρW_∞^2. Here, $p=p(\theta,z,t)$ is the pressure impressed on the boundary layer by the inviscid flow.

Equations (13)–(15) are subject to the following boundary conditions:

$$\left.\begin{aligned}u_\theta, u_z \quad \text{specified at}\quad t=0\quad \text{and as}\quad z\rightarrow\pm\infty,\\ u_r=u_\theta=u_z=0\quad \text{at}\quad y=0,\\ u_\theta\rightarrow U_\theta,\quad u_z\rightarrow U_z\quad \text{as}\quad y\rightarrow\infty,\\ u_\theta, u_z\quad \text{periodic in}\quad \theta,\end{aligned}\right\} \tag{17}$$

where U_θ and U_z are the inviscid velocity components in the θ- and z-directions respectively (Affes 1992). The initial conditions for u_θ and u_z are discussed just below. Far upstream and downstream, the boundary-layer solution corresponds to an impulsively started two-dimensional flow past a cylinder along with a Rayleigh boundary layer in the z-direction. Both of these flows are imbedded in the boundary and initial conditions. These conditions are chosen for convenience and since our interest in this work is the local viscous flow under the vortex, the basic results will not be greatly affected if other conditions are used.

To describe the motion subsequent to $t=0$, it is convenient to use the Rayleigh variable defined by

$$\eta=y/(2t^{1/2}),$$

and the governing equations (13)–(15) become

$$\frac{\partial u_r}{\partial \eta}+2t^{1/2}\frac{\partial u_\theta}{\partial \theta}+2t^{1/2}\frac{\partial u_z}{\partial z}=0, \tag{18}$$

$$4t\frac{\partial \boldsymbol{F}}{\partial t}-2\eta\frac{\partial \boldsymbol{F}}{\partial \eta}-\frac{\partial^2 \boldsymbol{F}}{\partial \eta^2}=-4t\boldsymbol{P}+\boldsymbol{R}, \tag{19}$$

where $\boldsymbol{F} = (u_\theta, u_z)$, $\boldsymbol{P} = (\partial p/\partial\theta, \partial p/\partial z)$, and $\boldsymbol{R} = (R_\theta, R_z)$, where

$$R_\theta = -4t\left(\frac{u_r}{2t^{1/2}}\frac{\partial u_\theta}{\partial \eta} + u_\theta\frac{\partial u_\theta}{\partial\theta} + (u_z - U_c)\frac{\partial u_\theta}{\partial z}\right), \tag{20}$$

$$R_z = -4t\left(\frac{u_r}{2t^{1/2}}\frac{\partial u_z}{\partial \eta} + u_\theta\frac{\partial u_z}{\partial\theta} + (u_z - U_c)\frac{\partial u_z}{\partial z}\right). \tag{21}$$

The initial conditions are obtained by taking the limit of (19) as $t \rightarrow 0$; this procedure is standard (Walker 1978; Affes & Conlisk 1993) and the initial conditions are

$$u_\theta^0 = U_\theta^0 \operatorname{erf}\eta, \tag{22}$$

and

$$u_z^0 = U_z^0 \operatorname{erf}\eta, \tag{23}$$

where the superscript 0 indicates $t = 0$. The solution for u_r^0 may be obtained analytically using the above expressions and the continuity equation and is given by

$$u_r^0 = -\left(\frac{\partial U_\theta^0}{\partial\theta} + \frac{\partial U_z^0}{\partial z}\right)\left(\eta\operatorname{erf}\eta + \frac{1}{\pi^{1/2}}e^{-\eta^2} - \frac{1}{\pi^{1/2}}\right). \tag{24}$$

For future reference, it is useful to investigate the induced vorticity field. In general, the vorticity field is defined as the curl of the velocity field and is given here in the original unscaled cylindrical coordinates as

$$\boldsymbol{\omega} = \frac{1}{r}\left\{\frac{\partial u_z}{\partial\theta} - r\frac{\partial u_\theta}{\partial z}\right\}\hat{\boldsymbol{i}}_r - \left\{\frac{\partial u_z}{\partial r} - \frac{\partial u_r}{\partial z}\right\}\hat{\boldsymbol{i}}_\theta + \frac{1}{r}\left\{\frac{\partial r u_\theta}{\partial r} - \frac{\partial u_r}{\partial\theta}\right\}\hat{\boldsymbol{i}}_z. \tag{25}$$

Using the boundary-layer-scaled variables defined above and dropping the terms of order $(Re^{-1/2})$ the scaled vorticity field takes a simpler form and is given by

$$Re^{-1/2}\boldsymbol{\omega} = \omega_\theta\hat{\boldsymbol{i}}_\theta + \omega_z\hat{\boldsymbol{i}}_z, \tag{26}$$

where ω_θ and ω_z are respectively the azimuthal and the axial scaled vorticity components given by

$$\omega_\theta = -\frac{1}{2t^{1/2}}\frac{\partial u_z}{\partial\eta}, \tag{27}$$

and

$$\omega_z = \frac{1}{2t^{1/2}}\frac{\partial u_\theta}{\partial\eta}. \tag{28}$$

Note that the scaled wall-shear components correspond to the components of scaled vorticity at the wall and thus may be given in terms of ω_θ and ω_z as

$$Re^{1/2}\tau_{r\theta} = \omega_z|_{\eta=0}, \tag{29}$$

and

$$Re^{1/2}\tau_{rz} = -\omega_\theta|_{\eta=0}. \tag{30}$$

4. Numerical methods

The numerical scheme used to solve the three-dimensional boundary-layer equations is a combination of finite-difference methods and Fourier transform methods. All of the calculations are performed in real variables. The Fourier transform method is employed to compute all derivatives with respect to θ. The derivatives with respect to z are obtained using a standard central finite-difference procedure in the calculation of the term $\partial u_z/\partial z$ appearing in the continuity equation and third-order upwind differencing to approximate the z-derivatives in the convective terms. In the η-direction, a coordinate transformation is employed to cluster the grid near the wall of the cylinder and central finite-difference formulae are applied to the resulting derivatives in the normal direction. Details of the computational procedure follow.

The coordinate transformation in the η-direction is performed by letting

$$\xi = g(\eta), \tag{31}$$

and if u denotes either velocity component u_θ or u_z, then by applying the Crank–Nicolson scheme in t to the momentum equations we obtain

$$4(t-\tfrac{1}{2}\Delta t)\frac{u^t-u^{t-\Delta t}}{\Delta t}-(\eta g'+\tfrac{1}{2}g'')\left(\frac{\partial u^t}{\partial \xi}+\frac{\partial u^{t-\Delta t}}{\partial \xi}\right)$$
$$-\tfrac{1}{2}g'^2\left(\frac{\partial^2 u^t}{\partial \xi^2}+\frac{\partial^2 u^{t-\Delta t}}{\partial \xi^2}\right)=\tfrac{1}{2}(P^t+P^{t-\Delta t}), \tag{32}$$

where
$$P=-4t(\partial p/\partial \theta)+R_\theta \tag{33}$$

for the θ momentum equation or

$$P=-4t(\partial p/\partial z)+R_z \tag{34}$$

for the z-momentum equation. The first and the second derivatives of u with respect to ξ are evaluated by using central differencing, and the final discretized form of the equations results in a tridiagonal system which may be written as

$$a_j u_{j-1}^{n+1}+b_j u_j^{n+1}+c_j u_{j+1}^{n+1}=-a_j u_{j-1}^{n}+d_j u_j^{n}-c_j u_{j+1}^{n}+e_j, \tag{35}$$

where
$$a_j=\tfrac{1}{2}(\eta_j g_j'+\tfrac{1}{2}g_j'')\frac{\Delta t}{\Delta \xi}-\tfrac{1}{2}g_j'^2\frac{\Delta t}{\Delta \xi^2}, \tag{36}$$

$$b_j=4t^{n+1/2}+g_j'^2\frac{\Delta t}{\Delta \xi^2}, \tag{37}$$

$$c_j=-\tfrac{1}{2}(\eta_j g_j'+\tfrac{1}{2}g_j'')\frac{\Delta t}{\Delta \xi}-\tfrac{1}{2}g_j'^2\frac{\Delta t}{\Delta \xi^2}, \tag{38}$$

$$d_j=4t^{n+1/2}-g_j'^2\frac{\Delta t}{\Delta \xi^2}, \tag{39}$$

and
$$e_j=\tfrac{1}{2}\Delta t(P^{n+1}+P^n). \tag{40}$$

A third-order upwind differencing scheme to treat the convective terms in the z-direction is employed in the present work and the method is described as follows. The third-order upwind differencing is illustrated for a typical convective term $f\partial u/\partial z$ by (Leonard 1984)

$$\left(f\frac{\partial u}{\partial z}\right)_i=\begin{cases} f_i(2u_{i+1}+3u_i-6u_{i-1}+u_{i-2})/6\Delta z+O(\Delta z^3) & \text{for } f_i>0 \\ f_i(-u_{i+2}+6u_{i+1}-3u_i-2u_{i-1})/6\Delta z+O(\Delta z^3) & \text{for } f_i<0, \end{cases} \tag{41}$$

which may be written in a more compact form as

$$\left(f\frac{\partial u}{\partial z}\right)_i=f_i\frac{-u_{i+2}+8u_{i+1}-8u_{i-1}+u_{i-2}}{12\Delta z}+|f_i|\frac{u_{i+2}-4u_{i+1}+6u_i-4u_{i-1}+u_{i-2}}{12\Delta z}+O(\Delta z^3). \tag{42}$$

Here the coordinate transformation used in η is given by

$$\eta = 2\xi/(1-\xi). \tag{43}$$

The implicit Crank–Nicolson marching technique is employed to advance the solution in time.

The Fourier transform of any flow quantity in the θ-direction is defined as

$$\bar{G}(m) = \int_{-\pi}^{\pi} G(\theta)\,\mathrm{e}^{-\mathrm{i}m\theta}\,\mathrm{d}\theta, \tag{44}$$

where $m = 0, \pm 1, \pm 2, \pm 3\ldots$ is the finite transform variable of θ. Here m ranges from $-M_\theta$ to M_θ. The discretization of the Fourier transform is carried out by definition of the discrete grid

$$-\pi \leqslant \theta \leqslant \pi, \quad \theta_i = (i-1-\tfrac{1}{2}M_\theta)\,\Delta\theta \quad \text{for} \quad i = 1,2,\ldots,M_\theta, \tag{45}$$

where the grid spacing $\Delta\theta$ should satisfy

$$\Delta\theta = 2\pi/M_\theta, \tag{46}$$

and M_θ is chosen to be of power 2 in order to efficiently use the fast Fourier transform (Cooley & Tukey 1965).

The iteration scheme consists of two main loops. In the outer loop, the boundary-layer equations are solved for each time step iteratively. The actual computational scheme solves for the perturbation from the initial condition (i.e. $\tilde{u}_z = u_z - u_z^0$ where u_z^0 is given by (23)) so that the convergence criterion is therefore somewhat tighter than for the solution of the total velocity field. At the beginning of each iteration, using the prescribed boundary conditions and pressure gradients which are known solutions of the potential flow, two subroutines are called to compute R_θ and R_z using values of $\tilde{u}_\theta$ and $\tilde{u}_z$ at the previous iterate as an initial guess. At the beginning of each time step, the values of R_θ and R_z are computed from the previous time step. As mentioned previously, the θ-derivatives in the convective terms are computed by taking the Fourier transform of the indicated quantity and then inverting to physical space; for example, the quantity $\mathrm{i}m\hat{u}_\theta$ is inverted for the calculation of $\partial\hat{u}_\theta/\partial\theta$. In the inner loop, we then sweep first in z and then in θ to solve the tridiagonal systems in η for the new iterates $\tilde{u}_\theta$ and $\tilde{u}_z$ using the Thomas algorithm. After each sweep of the mesh in z and θ, the convective terms are recalculated and the process is repeated until the change of $\tilde{u}_\theta$ or $\tilde{u}_z$ in successive iterations is less than a specified tolerance value; in this work a relative test with tolerance 10^{-4} is used for all the results. The calculation then continues to the outer loop where time marching is performed. In solving (19) under-relaxation is used according to the formulae

$$\tilde{u}_\theta = \Omega_\theta \tilde{u}_\theta^{new} + (1-\Omega_\theta)\,u_\theta^{old}, \quad \tilde{u}_z = \Omega_z \tilde{u}_z^{new} + (1-\Omega_z)\,\tilde{u}_z^{old},$$

where Ω_θ and Ω_z are the relaxation factors for $\tilde{u}_\theta$ and $\tilde{u}_z$ respectively. Initially, the relaxation factors are chosen to be 0.8 and the best results have been obtained by linearly reducing them to 0.4 in the latter stages of the calculations. In all cases in this work $\Delta\theta = 2\pi/32$ and $\Delta z = 0.1$ are used to generate the inviscid flow solutions.

It should be noted that since more grid points are required to resolve the boundary-layer calculations, in all cases studied here the inviscid flow results computed on the coarse grid are interpolated to give results on the finer grid. A cubic spline approximation is employed to represent the inviscid solution at points between the inviscid grid points giving an effective viscous grid size in the z-direction of 0.025. In addition, cubic spline interpolation is employed in the θ-direction to represent the inviscid flow solution on a finer viscous θ-grid. The inviscid flow solution is computed in a range $-12.8 \leqslant z \leqslant 12.8$ using a grid size $\Delta z = 0.1$. However, only the range $-1.5 \leqslant z \leqslant 1.5$, which contains 31 inviscid grid points, is required to compute the boundary-layer solution since the inviscid surface speeds and pressure gradients decay rapidly in z (figure 3). The z-range quoted above has been compared with larger domains in z with no change in the computed results.

In addition, since the time step employed to advance the vortex is larger than that required for the boundary-layer calculations, vortex positions are interpolated in time by repeatedly halving the time step until the new positions correspond to the required finer time step. Here a standard second-order interpolation scheme is used to obtain values at mid-intervals. The vortex positions are computed separately and then stored in a data file which is used to compute the inviscid flow field, pressure and pressure gradients at the cylinder surface.

The accuracy of the scheme has been checked by conducting a grid size study in ξ, z, θ and t. In all the results to be presented here, two-figure accuracy has been maintained up to time $t = 0.35$ for an (η, θ, z) grid corresponding to 61, 64 ($M_\theta = 32$), and 121 points, respectively with $\Delta t = 0.0025$. In addition, the boundary condition in the y-direction is imposed at a large but finite value of η, say $\eta = \eta_{max}$. In general, η_{max} is determined by testing larger values until the change in the results becomes negligible; $\eta_{max} = 6$ and 10 were tested and the value $\eta_{max} = 6$ is sufficient for three-digit accuracy.

5. Results

All the results to be presented here are for an (η, θ, z) grid corresponding to 61, 64, and 121 points. The streamlines in three-dimensional flow are obtained by solving the equations

$$\mathrm{d}\theta/u_\theta = \mathrm{d}y/u_r = \mathrm{d}z/u_z = \mathrm{d}S, \tag{47}$$

where S is a parameter that measures the distance along a given streamline. In the (z, η)-plane, for example, the above equations are numerically approximated according to

$$\eta - \eta_0 = \frac{u_{r0}}{2t^{1/2}}\Delta S, \quad z - z_0 = u_{z0}\Delta S \tag{48}$$

where (u_{r0}, u_{z0}) are the instantaneous velocities at an arbitrary initial point (η_0, z_0) at a given time t. Each streamline is traced by selecting a step ΔS according to (Hon & Walker 1987)

$$(u_z^2 + u_\theta^2 + u_r^2)\,\Delta S = 0.005. \tag{49}$$

It should be noted that because the points defining a streamline, in general, do not coincide with the mesh grid points, three-dimensional linear interpolation is used to compute the three velocity components. Some experimentation in the location of the origin of the streamlines is required, especially in the three-dimensional rendering to be described below. In this regard, to limit computer time a maximum of 3000 points along a streamline are plotted; thus those streamlines which appear to end in the fluid are the result of this arbitrary limiting procedure.

Figure 5 shows the results for the streamline patterns at several different times corresponding to $t = 0.1$, 0.2, 0.3 and 0.4. Note the development of a reversed-flow eddy which grows in time. By time $t = 0.3$ the eddy is developing rapidly and is characterized by a focus at the middle of the spiral (figure 5c); fluid entering the spiral passes out azimuthally as shown on figure 5(g, h) which show three-dimensional views

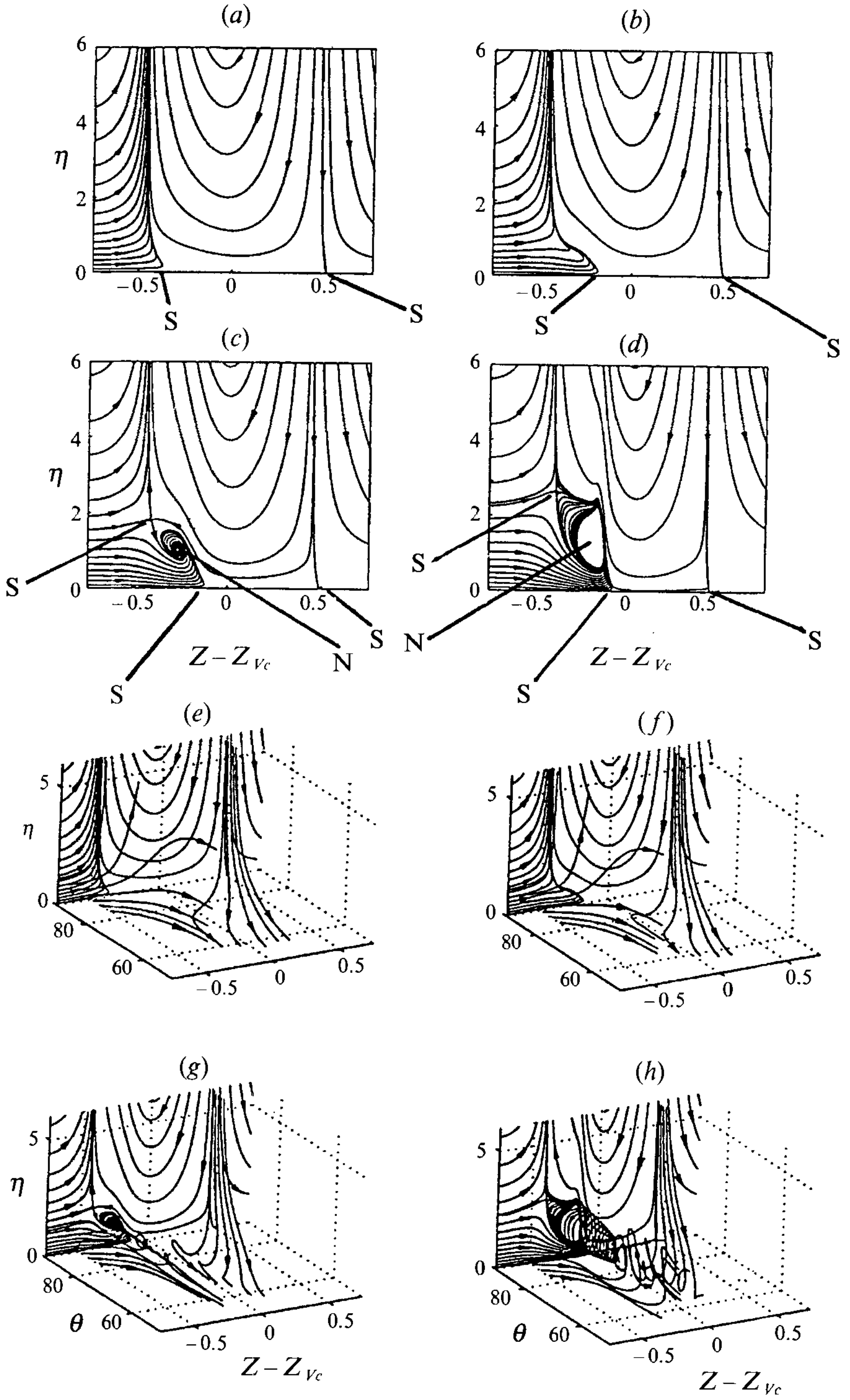

FIGURE 5. Streamline patterns for the symmetric mean flow plotted at various times: on the symmetry plane at (*a*) $t = 0.1$, (*b*) $t = 0.2$, (*c*) $t = 0.3$, (*d*) $t = 0.4$; and a fully three-dimensional view at (*e*) $t = 0.1$, (*f*) $t = 0.2$, (*g*) $t = 0.3$, (*h*) $t = 0.4$. The presence of singular points (N = node; S = saddle) is also shown.

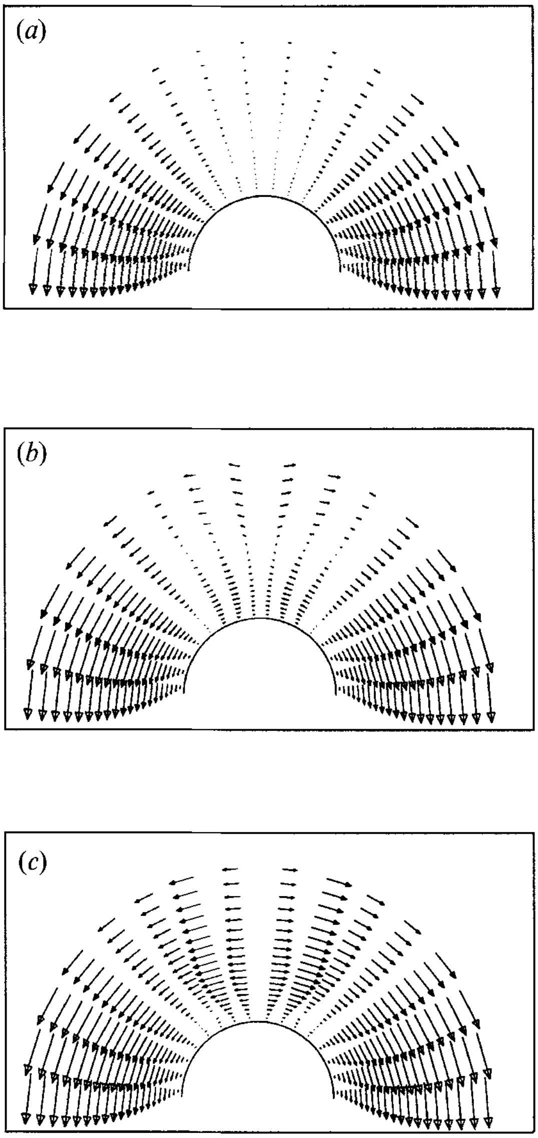

FIGURE 6. Vector plots of the velocity field at various locations in $Z-Z_{Vc}$ at $t = 0.4$ across the boundary layer. The upper edge is at $\eta = 2$; the edge of the boundary layer is at $\eta = 6$. (*a*) $Z-Z_{Vc} = -0.3$ (*b*) $Z-Z_{Vc} = -0.125$, (*c*) $Z-Z_{Vc} = 0$.

of the reversed flow region. The extent of the eddy roughly coincides with the region where the streamwise pressure gradient is of order -10 at time $t = 0.3$ when compared with figure 4. By $t = 0.4$ however, the eddy is considerably more developed. On figure 5 the presence of singular points (nodes and saddles in this case) is also indicated; these streamline patterns satisfy the topological constraint elucidated in rule 4 of Tobak & Peake (1982). It should also be mentioned that all of the streamlines that begin off the symmetry plane originate at about $\eta = 1$ far above the wall. These streamline patterns are depicted in the frame of reference travelling with the speed of the vortex head in the z-direction.

Figure 6 shows vector plots of the velocity field deep within the boundary layer on planes $z = Z-Z_{Vc}$ = constant at time $t = 0.4$. The upper edge of the field is at $\eta = 2$.

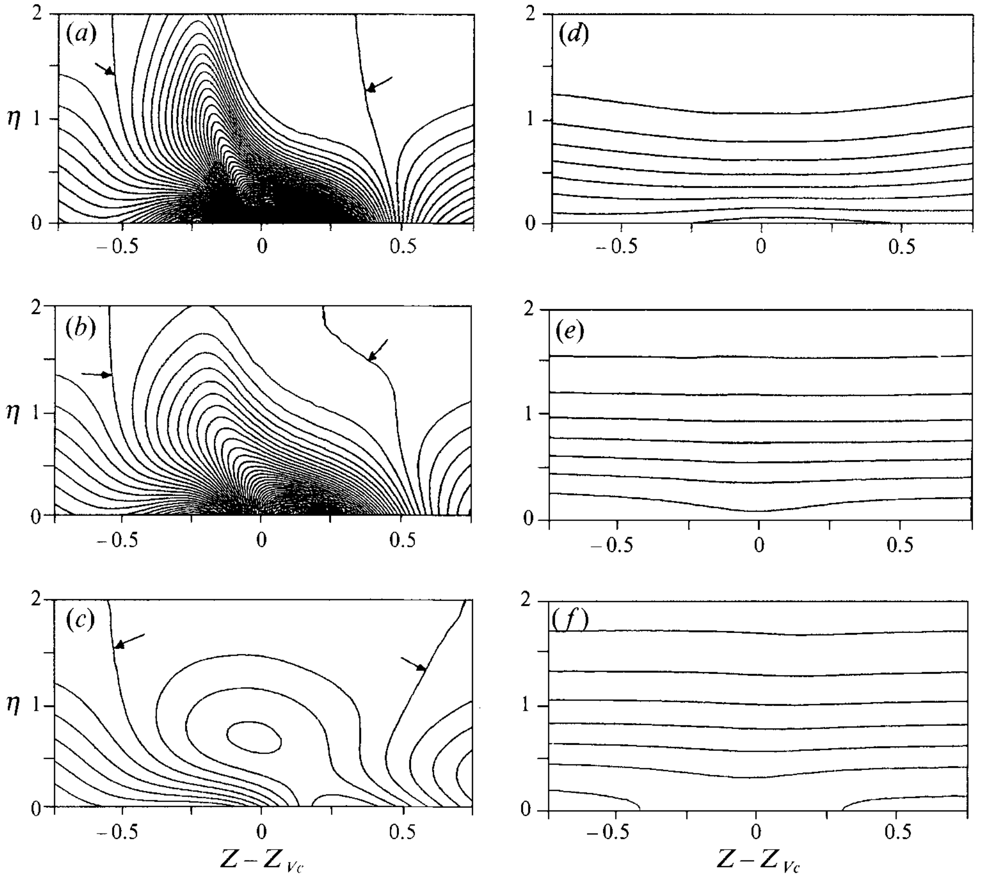

FIGURE 7. Lines of constant azimuthal vorticity ω_θ at $t = 0.3$ for several azimuthal locations around the cylinder: (*a*) $\theta = \pi/2$, (*b*) $\theta = 3\pi/8$, (*c*) $\theta = \pi/4$, (*d*) $\theta = 0$, (*e*) $\theta = -\pi/4$, (*f*) $\theta = -\pi/2$. The zero lines are marked by an arrow.

Note that the azimuthal velocity is toward the symmetry plane very near the wall and away from the symmetry plane farther above and that the flow to the symmetry plane occurs only locally in $z = Z - Z_{V_c}$ (figure 6*b*). This azimuthally reversed flow occurs below the streamline patterns depicted on figure 5(*h*) and is driven by a small adverse azimuthal pressure gradient which is present from the beginning of the calculation (figure 4). Note the complete absence of azimuthal reversed flow away from the symmetry plane on figure 6.

Figure 7 shows lines of locations of constant azimuthal vorticity ω_θ around the cylinder for time $t = 0.3$; note the concentration of azimuthal vorticity directly under the main vortex. The dark region corresponds to absolute values of the azimuthal vorticity above 1.2. The constant-azimuthal-vorticity lines for each of the values of θ on figure 7 are plotted in increments of 0.1 from -8 to 8. Figures 7(*a–f*) correspond respectively to distributions of the azimuthal vorticity across the boundary layer in the planes $\theta = \pi/2$, $3\pi/8$, $\pi/4$, 0, $-\pi/4$ and $-\pi/2$. On figure 7(*a–c*) the maximum positive azimuthal vorticity decreases from 7.90 to 0.432 while the negative azimuthal vorticity has dropped from -2.75 to -0.615. Positive values of the vorticity are associated with the development of the secondary eddy. For figure 7(*d–f*) the values of the azimuthal vorticity deep within the boundary layer are all negative and the maximum negative

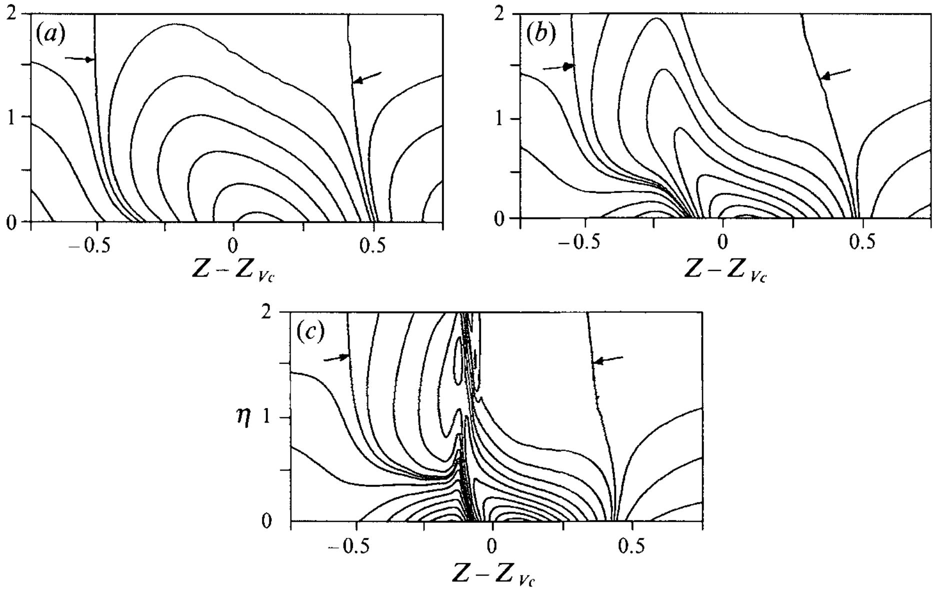

FIGURE 8. Temporal development of the azimuthal vorticity ω_θ in the symmetry plane $\theta = \pi/2$. These are lines of constant azimuthal vorticity which are plotted at various times: (*a*) $t = 0.1$, (*b*) $t = 0.2$, (*c*) $t = 0.4$. The zero lines are marked by an arrow.

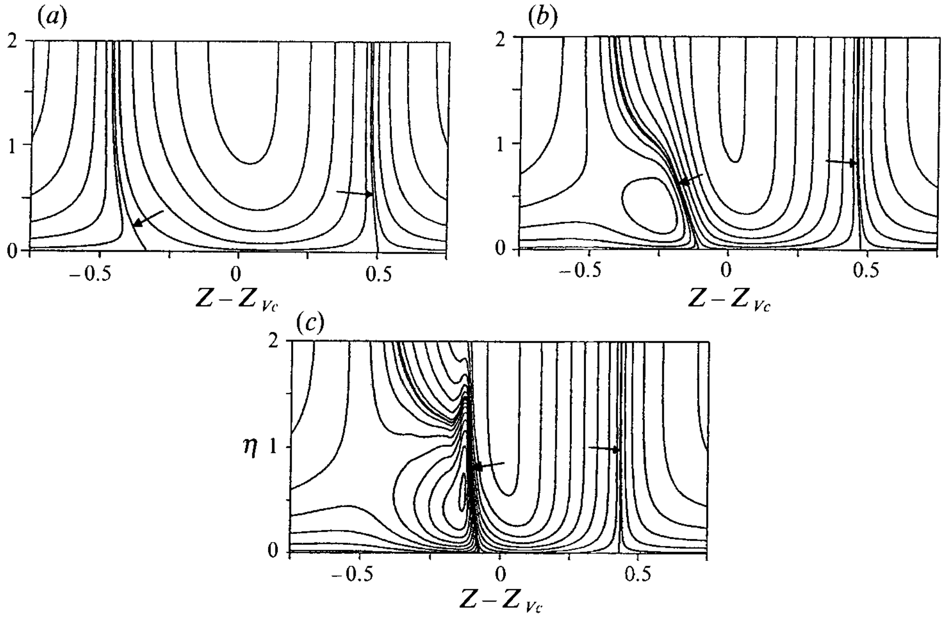

FIGURE 9. Lines of constant velocity u_z plotted across the boundary layer in the symmetry plane $\theta = \pi/2$ for various times: (*a*) $t = 0.1$, (*b*) $t = 0.3$, (*c*) $t = 0.4$. The zero velocity line is marked by an arrow.

value is -0.894 at $\theta = \pi/4$. Note that the maximum negative value of azimuthal vorticity at $\theta = -\pi/2$ is -0.732 which is close to that of $\theta = 0$; this indicates that in the bottom half of the cylinder the flow is dominated by the two-dimensional mean flow and the effects of the main vortex are small.

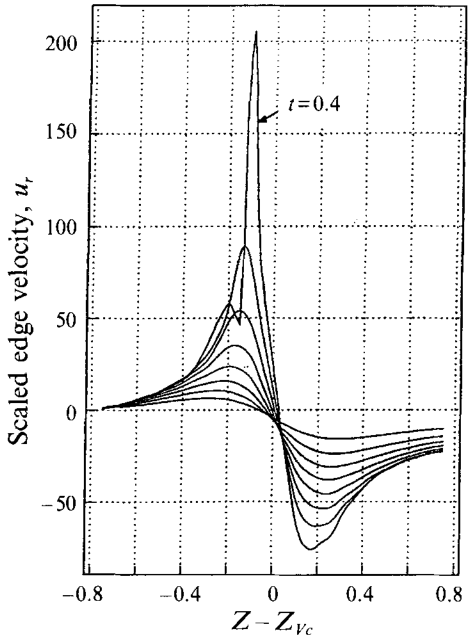

FIGURE 10. Temporal development of the radial velocity at the edge of the boundary layer evaluated in the symmetry plane $\theta = \pi/2$ at several times $t = 0.05, 0.1, 0.15, \ldots, 0.4$.

The time evolution of the azimuthal vorticity in the symmetry plane $\theta = \pi/2$ is shown on figure 8. Note the increasing focus of the lines in a narrow region just upstream of $z = 0$. It is well known that such behaviour may be a precursor of the occurrence of a singularity in the boundary-layer equations (Van Dommelen & Cowley 1990). The development of a singularity requires the vanishing of the vorticity vector in a coordinate system travelling with the local flow speed. It is seen on figure 8 that a zero azimuthal vorticity line is present in the vicinity of the focusing region. In the coordinate system travelling with the speed of the vortex head, the zero-azimuthal-vorticity line in this region tends, near the wall, to be very close to the zero-axial-velocity line shown on figure 9 and marked by an arrow. The axial vorticity is zero in the symmetry plane and thus, in the boundary-layer limit, the vorticity vector vanishes along the zero-azimuthal-vorticity line. This suggests that the singularity, if it occurs, may occur on the symmetry plane and this point is further discussed below.

On figure 10 the temporal development of the radial velocity is shown at $\theta = \pi/2$ for times $t = 0.05$ to 0.4 in increments of 0.05 plotted as a function of distance along the cylinder centreline. Note the rapid growth of the velocity as time increases; the result at time $t = 0.4$ should be viewed as qualitative near $z = 0$. The rapid growth of the displacement velocity in the region just upstream of the vortex head is reminiscent of the two-dimensional situation considered by Peridier *et al.* (1991*a*, *b*) and suggests a local breakdown of the boundary-layer approximation at a subsequent time.

Another view of the edge velocity showing the extremely local nature of the phenomenon is given on figure 11 where lines of constant radial velocity at the edge of the boundary layer around the cylinder are plotted for times $t = 0.1$, 0.2, 0.3 and 0.4. Note that at points significantly removed from $\theta = \pi/2$, the edge velocity varies somewhat more slowly than on the symmetry plane. The time evolution of the flow clearly shows rapid growth of the local magnitude of the edge velocity in a region

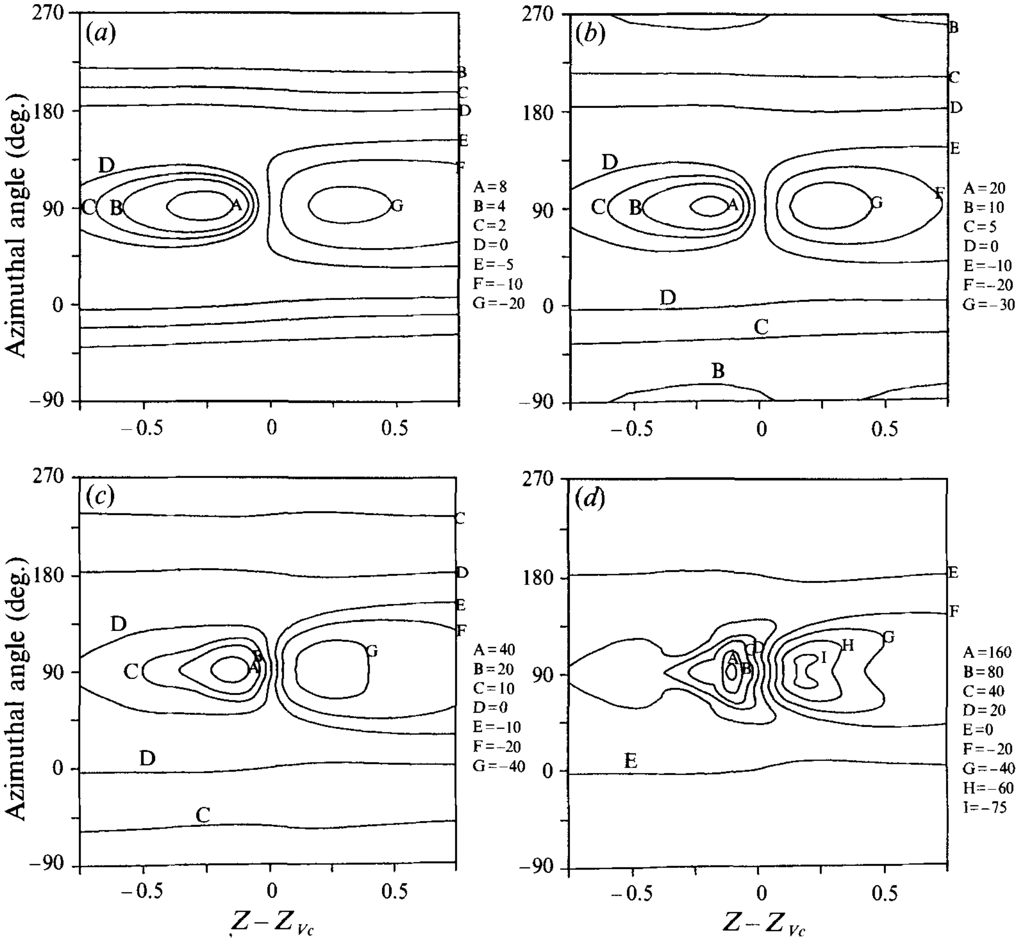

FIGURE 11. Lines of constant radial velocity u_r at the edge of the boundary layer plotted around the cylinder for various times. (*a*) $t = 0.1$, (*b*) $t = 0.2$, (*c*) $t = 0.3$, (*d*) $t = 0.4$. The values of u_r are shown.

extending off the symmetry plane and in which the location of very high radial velocity is continually contracting in the z-direction just upstream of $Z-Z_{Vc} = 0$. This behaviour suggests the physical picture of a wall of a three-dimensional non-circular jet of fluid which will be subsequently squeezed into the inviscid flow at a later time. This effect may be what Van Dommelen & Cowley (1990) refer to as a spreading ridge and a tongue of fluid.

Surface streamlines are shown on figure 12; there is initially a nodal point of separation at a position roughly coinciding with the front end of the eddy shown on figure 5. The single nodal point present at time $t = 0.1$ splits into a saddle point and two nodes. There is also a saddle point of attachment corresponding to the streamline which hits the wall just upstream of $z = Z-Z_{Vc} = 0.5$ on figure 5(*a–d*). This pattern satisfies the topological requirement the sum of the nodes and the sum of the saddles on a cylinder be the same; in general the sum of the nodes minus the sum of the saddles for an arbitrary surface is equal to the Euler characteristic χ ($\Sigma_N - \Sigma_S = \chi$) and for the cylinder $\chi = 0$ (Davey 1961; Flegg 1974, p. 97).

The vorticity components ω_θ and ω_z evaluated at the wall at $t = 0.4$ are shown on figures 13(*a*) and 13(*b*). Note that the zero-azimuthal-vorticity line indicated by the

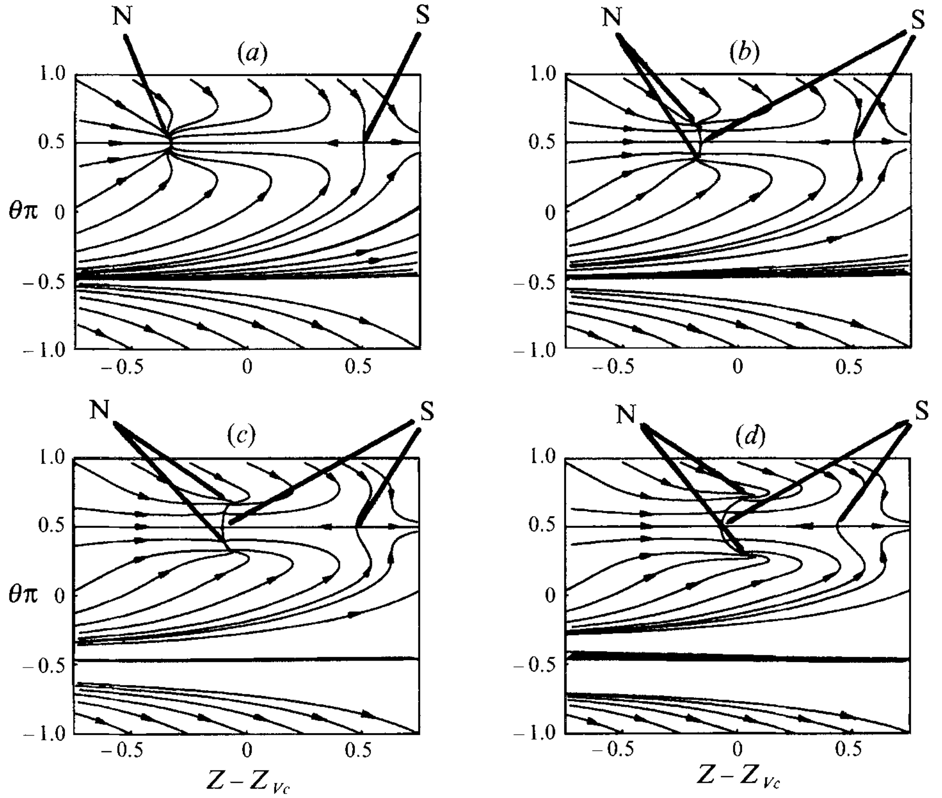

FIGURE 12. Surface streamlines at various times showing the splitting of a single node ($t = 0.1$) into a saddle point and two nodes. $\theta\pi = 0.5$ defines the symmetry line. (*a*) $t = 0.1$, (*b*) $t = 0.2$, (*c*) $t = 0.3$, (*d*) $t = 0.4$.

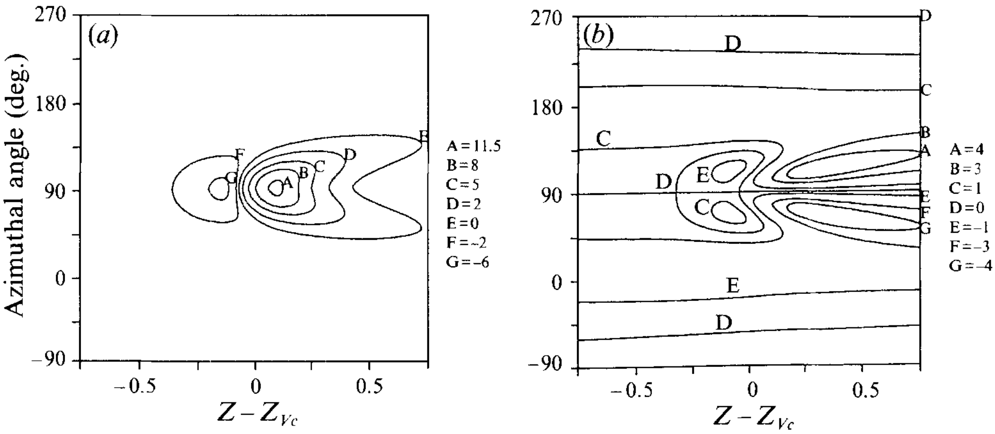

FIGURE 13. Lines of constant (*a*) azimuthal vorticity and (*b*) axial vorticity, evaluated at the wall of the cylinder and plotted for $t = 0.4$.

letter E on figure 13(*a*) is a closed line which is present for all times and only changes in shape as time increases. In particular, the major changes occur near the symmetry plane where the effects of the secondary flow become dominant especially at the later times. On the other hand, the lines of constant axial (streamwise) vorticity component

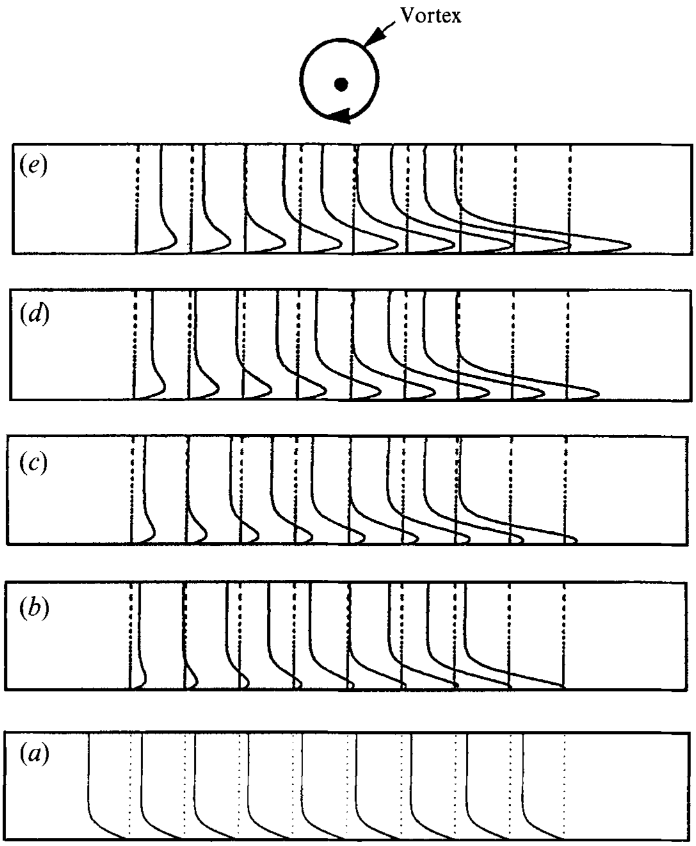

FIGURE 14. Temporal development of the velocity profiles of u_z plotted across the boundary layer ($0 \leqslant \eta \leqslant 6$) at various times: (*a*) $t = 0$, (*b*) $t = 0.15$, (*c*) $t = 0.2$, (*d*) $t = 0.25$, (*e*) $t = 0.3$. The profiles are shown at nine equally spaced locations which are centred around $z = Z - Z_{Vc} = -0.375$ and separated by $\Delta z = 0.025$.

ω_z depicted on figure 13(*b*) show the emergence of the zero line off the symmetry plane which is not present at $t = 0.1$ (not shown) and is denoted by the label D. There is also a line of $\omega_z = 0$ which spans the whole cylinder in the symmetry plane at $\theta = \pi/2$. This line exists at all times and is a result of the zero azimuthal velocity in the symmetry plane. Note that the region enclosed by the line $\omega_z = 0$ evolves to a horseshoe-like shape as depicted by figure 13(*b*).

On figure 14(*a–e*) the temporal development of the profiles of the velocity component u_z is shown. The axial velocity profiles are plotted at various times $t = 0$, 0.15, 0.2, 0.25, and 0.3. For each time the profiles are plotted at nine z-locations which are equally spaced and centred around the point $Z - Z_{Vc} = -0.25$. These results show the development of a forward flow region near the wall as time increases.

As noted by others (Van Dommelen 1981; Peridier *et al.* 1991*a*, *b*; Elliott, Cowley & Smith 1983), the solution to the boundary-layer equations in two dimensions in flows of this type will terminate in a singularity as time increases. Moreover, Van Dommelen & Cowley (1990) show that such a situation will occur in three dimensions as well. They state that a singularity in the boundary-layer equations will occur at the location of the simultaneous vanishing of a suitably defined Lagrangian coordinate and the vorticity vector. A necessary condition for this to occur is the presence of a line or surface where both the axial and azimuthal vorticity components vanish; moreover, it is clear that if

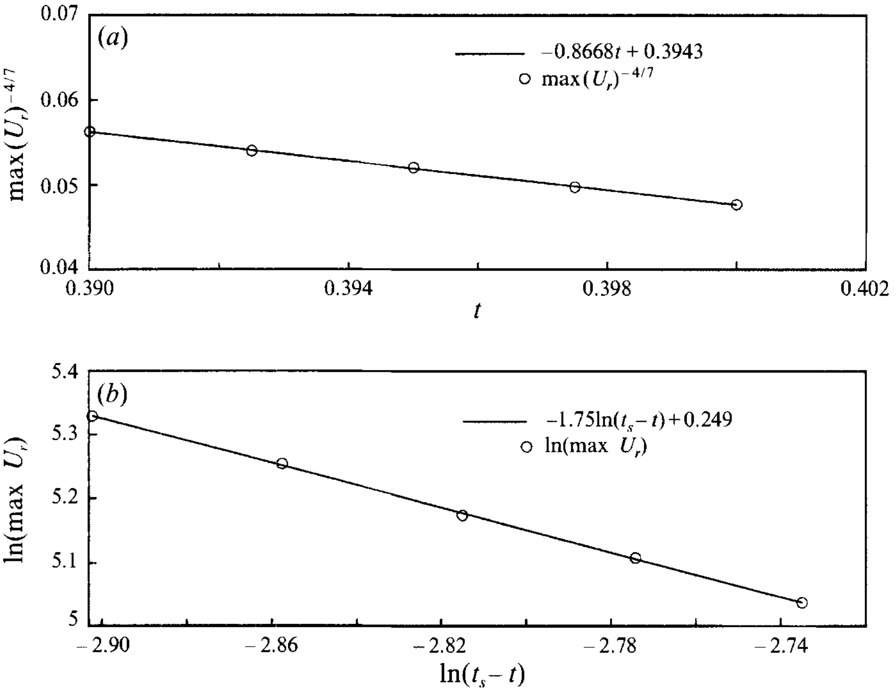

FIGURE 15. Emergence of the singularity in the boundary-layer equations: (*a*) $\max(u_{r,edge})^{-4/7}$ *vs.* time; (*b*) results of a least-squares curve fit to the numerical data for the times listed. t_s is calculated to be $t_s = 0.455$ for (*b*).

the location of such a line or surface is to originate deep within the boundary layer, both the azimuthal and axial components of the vorticity must change sign. In the present work, the zero-azimuthal-vorticity line can be easily located (figure 7). Since the axial component of the vorticity is zero in the symmetry plane $\theta = \pi/2$, the azimuthal vorticity in this plane represents the total vorticity. Consequently, it is plausible that a singularity in the boundary-layer equations will occur somewhere along the zero-azimuthal-vorticity line at $\theta = \pi/2$. This situation is consistent with the assertions of Van Dommelen & Cowley (1990) for the case of laterally symmetric flows in which the line along which the boundary layer is expected to erupt must either cross the symmetry line normally or coincide with it.

The Van Dommelen & Cowley (1990) work is generic in the sense that the development of a singularity depends on local flow properties and is independent of the precise geometry. Moreover, the variation of the flow in the cross-stream direction (here the θ-direction) is mild compared to the variation in the primary flow direction (z-direction) and the variation of the flow normal to the boundary (r-direction). Consequently, the singularity should develop in the manner described by Elliott *et al.* (1983). According to Elliott *et al.* (1983*a–c*) the maximum normal velocity at the edge of the boundary layer should behave as

$$\max(u_{r,edge}) \sim (t_s - t)^{-7/4}, \tag{50}$$

as the singular time is approached. If this is so, then the quantity $\max(u_{r,edge})^{-4/7}$ should approach zero linearly in $t_s - t$. Figure 15(*a*) shows this quantity plotted as a function of time in the latter stages of the calculation. From these results the singular time is determined by extrapolating the result of figure 15(*a*) to the point where $\max(u_{r,edge})^{-4/7}$

vanishes; this results in a singular time of $t_s = 0.455$. The results of the curve-fitting procedure depend somewhat on the length of the time frame chosen to perform the curve fit; the initial time chosen should be near enough to the singularity so that the structure can emerge. Additional results beginning at times just prior to $t = 0.39$ have been generated and the estimate of the singular time varies slightly; however, for all the domains chosen the linear behaviour depicted on figure 15 emerges. Figure 15(*b*) shows the result of a least-squares linear curve fit, which is given by

$$\max(u_{r,\,edge}) \sim 1.283(t_s - t)^{-1.751}; \tag{51}$$

note that the exponent is very close to the asymptotic value of $-7/4$. Similar results have been obtained by Wu & Shen (1992).

It should be noted that there are other locations away from $\theta = \pi/2$ where both components of vorticity vanish. These locations will, in general, occur on a line which results from the intersection of the zero-azimuthal-vorticity and the zero-axial-vorticity surfaces. However, since these locations are somewhat removed from the immediate location of the main vortex and the condition that the vorticity vector vanish is necessary but not sufficient for a singularity to develop, it is unclear whether these other locations where the vorticity vanishes are associated with an impending singularity.

6. Summary and conclusions

In the present paper, the three-dimensional boundary-layer flow due to a vortex impinging on a circular cylinder has been calculated. The inviscid flow has been assumed to be symmetric about the y-axis and this problem is a simplified model for the interaction of rotor tip vortex with an airframe. The main result of the paper is that a fully three-dimensional reversed-flow region develops under the impinging vortex and grows as the vortex approaches the cylinder. This reversed-flow region has been termed a secondary eddy and is characterized by locally high vorticity and swirling fluid motion with axis oriented approximately parallel to the axis of the vortex and extending about 20° on either side of the symmetry plane in the latter stages of the calculations. The eddy is viewed in a coordinate system moving with the speed of the centre point of the vortex.

Concurrent with the development of the secondary eddy is the rapid growth of the radial velocity at the top of the reversed-flow region. This rapid growth of the displacement velocity will occur whether or not the flow is symmetric with respect to the y-axis and, in the general situation, gives rise to the development of the three-dimensional separation ridge under the top of the vortex as depicted on figure 16. This separation ridge will continue to grow in time until the fluid is ejected into the main stream. In addition, the regime of rapid growth of the radial velocity is seen to undergo rapid contraction as time progresses, indicating the initiation of new length and time scales in the local flow prior to collision of the vortex with the airframe. In this regard, the present numerical computations can only capture the initial stages of the formation and development of the secondary eddy and the boundary-layer flow will terminate in a singularity as discussed in the previous section. Despite the fact that the inviscid calculation of the vortex position can be continued until the vortex is within about one vortex core radius, the viscous flow calculations cannot be continued accurately beyond the point where the vortex is about two core radii from the cylinder.

Two further comments are appropriate. First, the dimensionless vortex strength in this work has been taken to be 4.18, a value which is partially motivated by the values of the dimensional circulation estimated from the experiments of Liou *et al.* (1990).

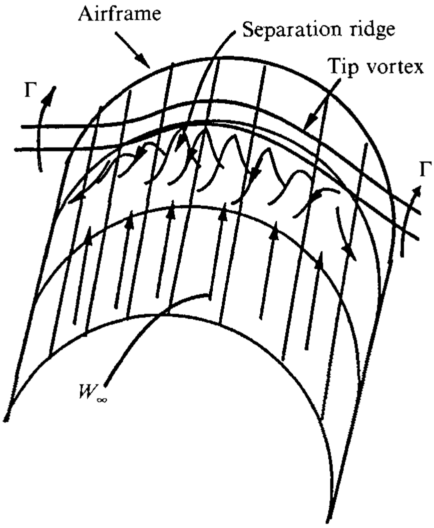

FIGURE 16. The physical picture of the erupting three-dimensional boundary layer on a cylinder indicated by the present calculations.

This strength is relatively large, and from a fundamental point of view it is natural to inquire how the present results will be modified with a weaker vortex. It is also useful to point out that the configuration of the rotorcraft experiments at Maryland (Bi & Leishman 1990) may, to a first approximation, be modelled by merely switching the sign of the circulation (Affes & Conlisk 1993). In this case, an eruptive region is likely to form just ahead of the main vortex with the evolution of the secondary flow being similar. Second, in the present configuration where the vortex is impinging on the airframe a significant adverse pressure gradient has formed at the same time as the reversed flow is growing. This is in contrast to the two-dimensional case considered by Doligalski & Walker (1984) where the adverse pressure gradient is not particularly large and is independent of time. In that work the vortex is travelling parallel to the wall and eruptive behaviour develops; it is likely that the presence of a significant adverse pressure gradient in flows of this type will hasten the eruptive process.

The authors appreciate the support of the US Army Research Office under contract DAAL03-K-0095. The contract monitor is Dr Thomas L. Doligalski. The authors are grateful to The Ohio Supercomputer Center for a grant of computer time to perform these calculations. Many helpful suggestions on all aspects of this work have been provided by O. R. Burggraf.

REFERENCES

AFFES, H. 1992 Tip-vortex–airframe interactions. PhD thesis, The Ohio State University.

AFFES, H. & CONLISK, A. T. 1991 The unsteady interaction of a three-dimensional vortex filament with a cylinder. *Proc. Intl Specialists' Meeting on Rotorcraft Basic Research, Georgia Institute of Technology, March 25–27, 1991*, pp. 37-1–37-11.

AFFES, H. & CONLISK, A. T. 1993 A model for rotor tip vortex–airframe interaction Part 1: Theory. *AIAA J.* **31**, 2263–2273.

AFFES, H., CONLISK, A. T., KIM, J. M. & KOMERATH, N. M. 1993 A model for rotor tip vortex–airframe interaction Part 2: Comparison with experiment. *AIAA J.* **31**, 2274–2282.

BATCHELOR, G. K. 1967 *Introduction to Fluid Dynamics*. Cambridge University Press.

BI, NAI-PEI & LEISHMAN, J. G. 1990 Experimental study of rotor/body aerodynamic interactions. *J. Aircraft* **27**, 779–788.

BRAND, A. G., MCMAHON, H. M. & KOMERATH, N. M. 1990 Correlations of rotor wake/airframe interaction measurements and flow visualization data. *J. Am. Hel. Soc.* **10**, 4–15.

CHUANG, F. S. & CONLISK, A. T. 1989 The effect of interaction on the boundary layer induced by a convected rectilinear vortex. *J. Fluid Mech.* **200**, 337–365.

COOLEY, J. W. & TUKEY, J. W. 1965 An algorithm for the machine calculation of complex Fourier series. *Maths. Comput.* **19**, 297–300.

DAVEY, A. 1961 Boundary-layer flow at a saddle point of attachment. *J. Fluid Mech.* **10**, 593–610.

DHANAK, M. R. 1981 Interaction between a vortex filament and an approaching rigid sphere. *J. Fluid Mech.* **109**, 129–147.

DOLIGALSKI, T. L. & WALKER, J. D. A. 1984 The boundary layer induced by a convected rectilinear vortex. *J. Fluid Mech.* **139**, 1–30.

ELLIOTT, J. W., COWLEY, S. J. & SMITH, F. T. 1983 Breakdown of boundary layers: i. on moving surfaces; ii. in semi-similar flow; iii. in fully unsteady flow. *Geophys. Astrophys. Fluid Dyn.* **25**, 77–138.

ERSOY, S. & WALKER, J. D. A. 1985 The viscous flow induced near the wall by counter-rotating vortex pairs and vortex loops. *Rep.* FM-8. Lehigh University.

FLEGG, G. C. 1974 *From Geometry to Topology*. Crane, Russak & Co. Inc.

HARVEY, J. K. & PERRY, F. J. 1971 Flowfield produced by trailing vortices in the vicinity of the ground. *AIAA J.* **9**, 1659–1660.

HON, L. & WALKER, J. D. A. 1987 An analysis of the motion and effects of hairpin vortices. *Rep.* FM-11. Dept. of Mechanical Engineering and Mechanics, Lehigh University.

LARMOR, J. 1889 Electromagnetic and other images in spheres and planes. *Q. J. Pure Appl. Maths* **23**, 94–101.

LEONARD, B. P. 1984 Third-order upwinding as a rational basis for computational fluid dynamics. In *Computational Techniques & Applications: CTAC-83* (ed. J. Noye & C. Fletcher). Elsevier.

LEWIS, T. C. 1879 On the images of vortices in a spherical vessel. *Q. J. Pure Appl. Maths* **16**, 338–347.

LIGHTHILL, M. J. 1957 The image system of a vortex element in a rigid sphere. *Camb. Phil. Soc.* **52**, 317–321.

LIOU, S. G., KOMERATH, N. M. & MCMAHON, H. M. 1990 Measurement of the interaction between a rotor tip vortex and a cylinder. *AIAA J.* **28**, 975–981.

MOORE, D. W. 1972 Finite amplitude waves on aircraft trailing vortices. *Aero. Q.* **23**, 307–314.

PERIDIER, V., SMITH, F. T. & WALKER, J. D. A. 1991*a* Vortex-induced boundary layer separation. Part 1. The unsteady limit problem. $Re \rightarrow \infty$. *J. Fluid Mech.* **232**, 99–131.

PERIDIER, V., SMITH, F. T. & WALKER, J. D. A. 1991*b* Vortex-induced boundary-layer separation. Part 2. Unsteady interacting boundary-layer theory. *J. Fluid Mech.* **232**, 133–165.

SARPKAYA, T. 1989 Computational methods with vortices – The 1988 Freeman Scholar Lecture. *Trans. ASME* I: *J. Fluids Engng* **111**, 5–52.

SHERIDAN, P. F. & SMITH, R. F. 1980 Interactional aerodynamics – a new challenge to helicopter technology. *J. Am. Hel. Soc.* **25**, No. 1, January.

TOBAK, M. & PEAKE, D. J. 1982 Topology of three-dimensional separated flows. *Ann. Rev. Fluid Mech.* **14**, 61–85.

VAN DOMMELEN, L. L. 1981 Unsteady boundary-layer separation. PhD dissertation, Cornell University.

VAN DOMMELEN, L. L. & COWLEY, S. J. 1990 On the Lagrangian description of unsteady boundary-layer separation. Part 1. General theory. *J. Fluid Mech.* **210**, 593–626.

WALKER, J. D. A. 1978 The boundary layer due to a rectilinear vortex. *Proc. R. Soc. Lond.* A **359**, 167–188.

WALKER, J. D. A., SMITH, C. R., CERRA, A. W. & DOLIGALSKI, T. L. 1987 The impact of a vortex ring an a wall. *J. Fluid Mech.* **181**, 99–140.

WU, T. & SHEN, S.-F. 1992 Emergence of three-dimensional separation over a suddenly started prolate spheroid at incidence. *AIAA J.* **30**, 2707–2715.